Journal of
Synchrotron
Radiation

ISSN 0909-0495

Received 27 July 2011
Accepted 13 October 2011

Status of the hard X-ray microprobe beamline ID22 of the European Synchrotron Radiation Facility

Gema Martínez-Criado,* Rémi Tucoulou, Peter Cloetens, Pierre Bleuet, Sylvain Bohic, Jean Cauzid, Isabelle Kieffer, Ewelina Kosior, Sylvain Labouré, Sylvain Petitgirard, Alexander Rack, Juan Angel Sans, Jaime Segura-Ruiz, Heikki Suhonen, Jean Susini and Julie Villanova

European Synchrotron Radiation Facility, Experiments Division, 38043 Grenoble, France.
E-mail: gmartine@esrf.fr

The ESRF synchrotron beamline ID22, dedicated to hard X-ray microanalysis and consisting of the combination of X-ray fluorescence, X-ray absorption spectroscopy, diffraction and 2D/3D X-ray imaging techniques, is one of the most versatile instruments in hard X-ray microscopy science. This paper describes the present beamline characteristics, recent technical developments, as well as a few scientific examples from recent years of the beamline operation. The upgrade plans to adapt the beamline to the growing needs of the user community are briefly discussed.

Keywords: X-ray microprobe; X-ray nanoprobe; X-ray fluorescence; microspectroscopy.

1. Introduction

Among the 40 beamlines in operation at the European Synchrotron Radiation Facility, ID22 is fully dedicated to hard X-ray microanalysis consisting of the combination of X-ray fluorescence (XRF), X-ray absorption spectroscopy (XAS), X-ray diffraction (XRD) and X-ray imaging (XRI) techniques in the hard multi-keV X-ray regime (Somogyi *et al.*, 2005). The beamline is composed of two experimental stations, which permit studies in several research fields such as medicine, biology, earth and planetary sciences, environmental science, archaeometry and materials science. These disciplines seek non-destructive investigation of the spatial distribution, concentration and speciation of trace elements to be correlated to the morphology and crystallographic orientations at the (sub)micrometre levels. Both stations share a common instrumental set-up: an X-ray focusing device, a high-precision stage to raster the sample on the beam, a visible-light microscope (VLM) to visualize the regions of interest of the samples, as well as some detection schemes and 2D/3D XRI approaches.

After several years refining the analytical methods, hard X-ray focusing devices, positioning stages and detection schemes, two hutches are clearly defined today by their spatial resolution: EH1 devoted to microanalysis and EH2, also known as ID22 nano-imaging station (ID22NI), exclusively used for nanoanalysis (see Table 1). The stations offer a large variety of well established approaches:

(i) EH1: scanning-XRF and XRF-tomography, micro-XAS and XANES imaging, X-ray excited optical luminescence, linear dichroism, scanning XRD, absorption/phase contrast tomography, and diffraction-tomography.

(ii) EH2-ID22NI: scanning-XRF and XRD, XRF- and XRD-tomography, X-ray projection microscopy, full-field magnified tomography, and coherent scanning X-ray diffraction.

The flexible design, long working distances and high penetration powers also allow the integration and development of different controlled sample environments in EH1. A few examples include anvil cells, microfurnace, He chamber, cryostreams as well as other environments routinely integrated in the beamline (LINKAM HSF91 stage for heating and freezing applications, He mini-cryostat, *etc*). An additional development to be shared between both stations is the confocal XRF mode using a polycapillary half-lens pioneered by the MiTAC group (Vincze *et al.*, 2004). In the next section the major technical upgrades recently performed at ID22 are summarized.

2. ID22 instrumentation

2.1. X-ray source

Currently the high-β straight section of ID22 is equipped with two insertion devices: an in-vacuum U23 and a revolver U35/U19. Table 2 summarizes the main parameters for both undulators. The photon flux emitted by both devices is presented in Fig. 1, calculated at 30 m from the source through a 0.5 mm $\times$ 0.5 mm pinhole (the insertion device U42 is depicted for reference purposes only). The electron beam characteristics included a current of 200 mA, an energy of 6 GeV and a relative energy spread of 0.001. The vertical (horizontal) emittance, β values and dispersion are 39 pm (3.9 nm), 3 m (37.2 m) and zero (0.137 m), respectively. The

Table 1
Main characteristics of ID22 end-stations.

	EH1	EH2-ID22NI
Spatial resolution (μm)	1 × 4	0.065 × 0.050
Focusing optics	KB mirrors	KB mirrors
Maximum flux (photons s^{-1})	5×10^{11}	2×10^{12}
Energy range	6.5–65 keV	17 and 29 keV
Techniques	XRF, XAS, XRD XRI-2D/3D	XRF, XRD XRI-2D/3D

revolver device was chosen to give maximum photon output in a very narrow energy range centred on 17.5 keV that is the principal working energy at ID22NI. It has at least the same performance as a conventional U42 undulator in terms of gap reproducibility and speed. The device is equipped with a tunable undulator (U35) and a dedicated (optimized) low-*K* undulator specific to the needs of the beamline (U19). The switching between one undulator to the other takes about 2 min including the opening of the gap to 250 mm, the rotation of the girders, and the gap closure with the revolver undulator to 11 mm. It is almost transparent to the user. The availability of two interchangeable magnetic structures (35 and 19 mm period) combined with the U23 in-vacuum undulator allows for better optimization of the X-ray photon flux for various energy ranges, overcoming the old configuration based on a U42 undulator, which created an energy gap between 15 and 18 keV.

2.2. End-station EH1

2.2.1. Microprobe set-up. An overview of the experimental arrangements of ID22 end-stations is depicted in Fig. 2. The end-station EH1 has two parts: the full-field tomography table and the microprobe set-up. In order to explore the merits of high energy (up to 65 keV), a special pair of crossed mirrors in Kirkpatrick–Baez (KB) configuration is installed at the microprobe set-up (Borchert *et al.*, 2010). It comprises two

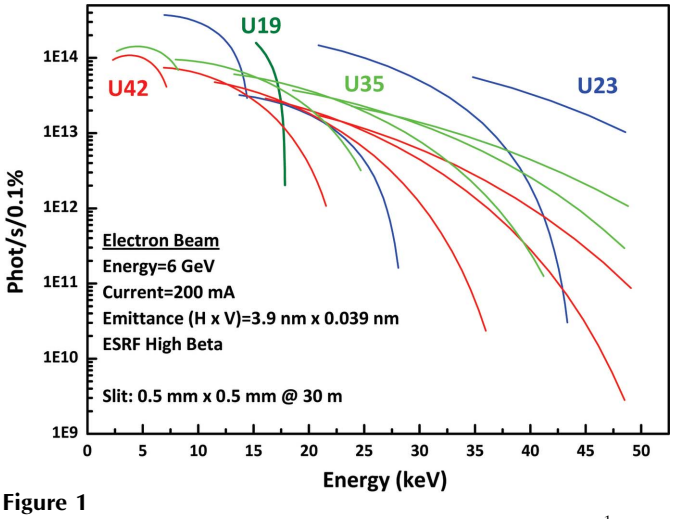

Figure 1
The output spectra of the undulators of ID22 shown as photons s^{-1} (0.1% bandwidth)$^{-1}$ through a 0.5 mm (H) × 0.5 mm (V) pinhole at 30 m (equivalent to the position and normal slit gaps of the primary slits) from the centre of the undulator. U42 is shown for reference purposes only.

Table 2
Summary of the relevant parameters of the revolver undulator U35/19 and the in-vacuum undulator U23.

Insertion device	U35/19	U23
Period (mm)	35/19	23
Length (mm)	1.6	2.0
Magnet material	NdFeB	Sm_2Co_{17}
Minimum gap (mm)	11	6
Peak field at minimum gap, I = 200 mA (T)	0.74/0.32	0.78
Power density at 30 m, minimum gap, I = 200 mA (W mm^{-2})	97/82	181

elliptically shaped Si mirrors, a 170 mm-long mirror focusing at a distance of 390 mm from the centre of the mirror in the vertical direction, and a 92 mm-long mirror with a 190 mm focusing distance in the horizontal direction. They are coated with graded multilayers (B4C/[W/B4C]40/Cr), playing both monochromatization and focusing roles. Four actuators (μ-Focus picomotors) bend the flat polished mirrors (CoastLine Optics) into the elliptical figures required for imaging the X-ray source. Both arms of each bender are equipped with linear encoders (Mercury 3500). This design provides reflectivity of 96% at 65 keV and 75% at 8 keV. Thus, we can exploit both pink and monochromatic beam operations based on

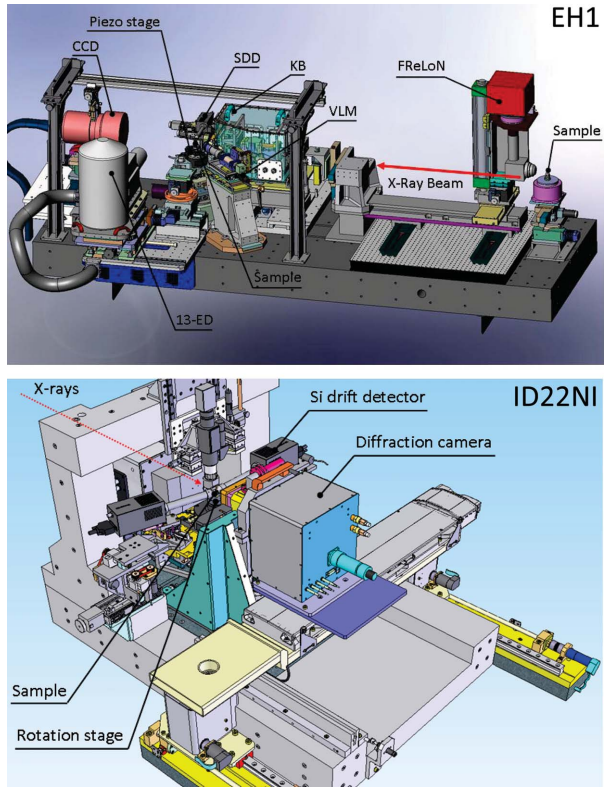

Figure 2
Overview of the experimental arrangements of ID22 end-stations EH1 and ID22NI. The upper part illustrates the EH1 end-station: on the right is the full-field tomography set-up, and on the left is the microprobe. The lower part depicts the ID22NI end-station. The direction of the X-ray beam is also indicated. KB represents the Kirkpatrick–Baez mirrors, 13-ED the 13-element detector, SDD the Si drift detector, and VLM the visible light microscope.

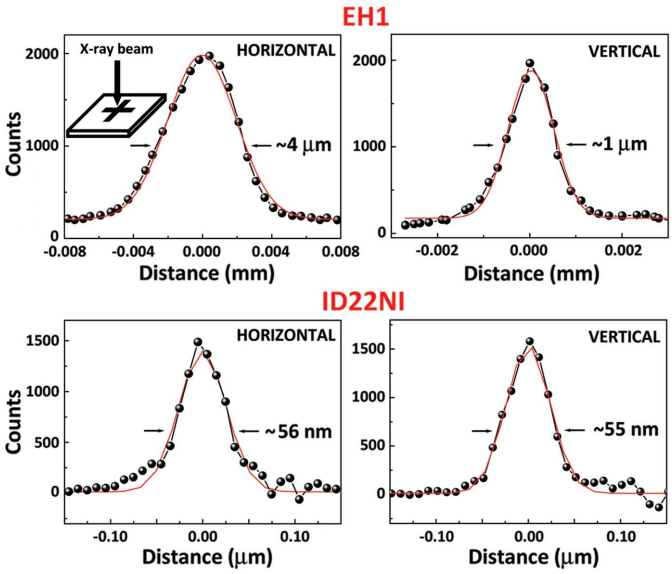

Figure 3
Focused beam profiles taken at 12 and 17 keV in EH1 (upper part) and ID22NI (lower part) by means of Ni and Au knife-edge scans, respectively. Solid circles represent the raw data and solid lines represent the respective Gaussian fits.

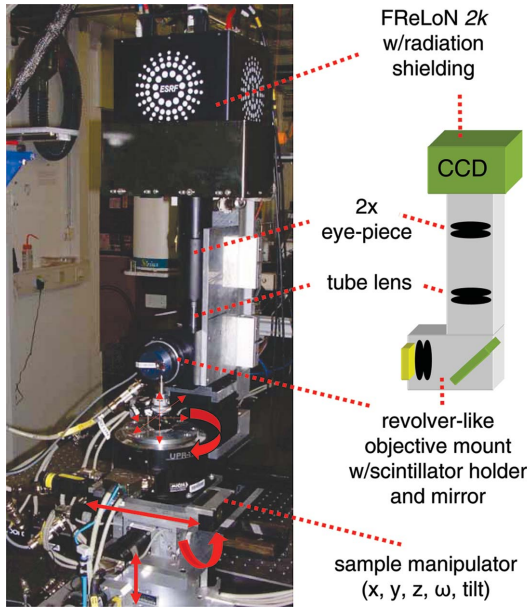

Figure 4
Photograph of the microtomography station in EH1. The sketch shows the classical layout of a high-resolution indirect X-ray detector compromising a scintillator screen, visible-light optics and a digital camera (Weitkamp *et al.*, 1999). For alignment purposes the FReLoN 2k camera is mounted on a rotation stage (not shown in the sketch), and the sample-to-detector distance can be changed between approximately 6 and 800 mm.

Bragg diffraction and total external reflection modes, respectively. The pink beam approach uses the standard multilayer configuration to increase beam divergence (numerical aperture), producing a very high photon flux (10^{12} photons s^{-1}). The second strategy optimized for spectroscopic acquisitions relies on grazing incidence to provide a monochromatic beam flux of about 5×10^{10} photons s^{-1}. In the high-energy range, the beamline is well equipped. First, the in-vacuum undulator provides a high photon flux, and, second, the Kozhu double-crystal monochromator, which can cover an angular range from 2.6 to 32.5° [*i.e.* 3.7 to 43.5 keV energy range for Si(111), and 7.1 to 83.5 keV for Si(311)]. The resulting spot size at the focal plane of about 1 μm × 4 μm (V × H) is shown in the upper part of Fig. 3.

2.2.2. Full-field tomography set-up. Fig. 4 shows the full-field micro-tomography set-up, which is located upstream from the focusing optics on EH1 (Weitkamp *et al.*, 1999). This retractable stage provides complementary information and is often used preliminarily to investigate specimens (*e.g.* to select a specific region of interest within a larger object and/or to select the most representative of a number of samples). The full set-up is mounted on a table and a high-precision linear stage that guarantees not only repeatability but also an easy and quick switch with the microprobe (Artioli *et al.*, 2010). The system includes the high-precision air-bearing rotation stage UPR-160Air (miCos GmbH), the tilt, the vertical translation stage, and the CCD camera ESRF standard FReLoN 2k 14-bit (Labiche *et al.*, 2007). The readout speed of the FReLoN detector depends drastically on the operation mode (full-frame, frame transfer, kinetics pipeline), binning, dynamic range and the region of interest. The most frequently employed mode gives about 100 ms readout time without region-of-interest or binning (Labiche *et al.*, 2007). Similarly, the spatial resolution depends on the scintillator screen (Martin *et al.*, 2009) and the numerical aperture of the objective, as well as the effective pixel size used. Frequently, it is adapted together with the desired field of view and can reach up to the submicrometre range. For the reconstruction of the tomographic images the filtered-backprojection algorithm is used *via* the ESRF software package *PyHST* (http://www.esrf.eu/UsersAndScience/Experiments/TBS/SciSoft/).

2.3. End-station EH2-ID22NI

2.3.1. Nanoprobe set-up. Located at 64 m from the source, the nanofocusing optics consist of two graded multilayer coated surfaces mounted in crossed KB configuration (Morawe *et al.*, 2006). It is composed of a 112 mm-long mirror focusing at a distance of 180 mm from the centre of the mirror in the vertical direction and a 76 mm-long mirror with an 83 mm focusing distance in the horizontal direction. Four actuators (μ-Focus picomotors) bend the flat polished mirrors (CoastLine Optics) into the elliptical figures required for imaging the X-ray source. Both arms of each bender are equipped with linear encoders (Mercury 3500). This design provides reflectivity of 73% at 17 keV and 74% at 8 keV. The resulting spot size at the focal plane of about 60 nm × 60 nm (V × H) is shown in the lower part of Fig. 3. The vertical mirror images the undulator source (∼25 μm FWHM), whereas a virtual source is created in the horizontal direction using the high-heat-load slits (depending on the spatial resolution and photon flux required by the experiment, from 10

Table 3
Summary of the relevant characteristics of the KB systems.

KB system	EH1	EH2-ID22NI
Lengths, V × H (mm)	170 × 92	112 × 76
Material	Si	Si
Coating	$B_4C/[W/B_4C]_{40}/Cr/Si$	$B_4C/[W/B_4C]_{25}/Cr/Si$
Source distance, p (m)	41	64
Focal lengths, V × H, q (m)	0.390 × 0.190	0.180 × 0.083
Incidence angles, V × H (mrad)	2.5 × 3.5 at 65 keV 10.7 × 15.1 at 15 keV	8.1 × 8.2 at 17 keV 4.8 × 4.8 at 29 keV
Spot size (µm)	1 × 4	0.060 × 0.060

up to 25 µm). The multilayer mirrors play both the role of focusing device and monochromator, resulting in a very high flux of about 5×10^{12} photons s^{-1} and medium monochromaticity of $\Delta E/E \simeq 10^{-2}$. Invar, as material of choice for the benders, has improved the thermal stability (Tucoulou *et al.*, 2008) and, in particular, the stability of the incident angles and curvature of the elliptically shaped mirrors. A complete description of the nanofocusing optics and nano-imaging station can be found elsewhere (Barrett *et al.*, 2011; Hignette *et al.*, 2007; Zhang *et al.*, 2010; Cloetens *et al.*, 2012).

The main characteristics of previous focusing systems are listed in Table 3.

2.3.2. Polycapillary optics. Polycapillary optics in confocal detection geometry can be used as a spatial filter for all applications in which background radiation, from areas not in the region of interest, interferes with the signal under study. XOS monolithic polycapillary optics optimized to a working distance of 2.5 mm and a cut-off energy of 15 keV is available at the beamline with a transmission efficiency of about 2.5% at 15 keV. Thus, the spontaneous radiation background is practically eliminated from the spectrum and therefore the detection sensitivity and accuracy is greatly improved. Also, buried structures can be studied by depth-sensitive X-ray absorption spectroscopy in fluorescence detection mode at the micrometre scale. In summary, these lenses can be used in our scanning fluorescence microscopes for high-resolution two-dimensional mapping, as well as confocal XAS acquisitions, 3D XRI and XRF tomography experiments.

2.4. Sample environments

2.4.1. HP and HT diamond anvil cell. Within the framework of a close collaboration with the Laboratoire des Sciences de la Terre (ENS-Lyon, France), a diamond anvil cell dedicated to XRF analysis under high pressure and high temperature was drafted, built and tested at EH1 (Petitgirard *et al.*, 2009), allowing *in situ* geochemical studies of heavy elements, rare earth elements (REE), and first transition metals at p.p.m. concentration levels. The designed system enables XRF detection at 90° from the incident beam using the thermally isolated 13-element Si(Li) solid-state detector located 50 mm from the sample position. Elements like Rb, Sr, Y and Zr with concentrations as low as 50 p.p.m. were detected with the cell operating at 5.6 GPa and 1273 K. Its vacuum chamber (10^{-3} mbar) presents an optimized shielding and collection

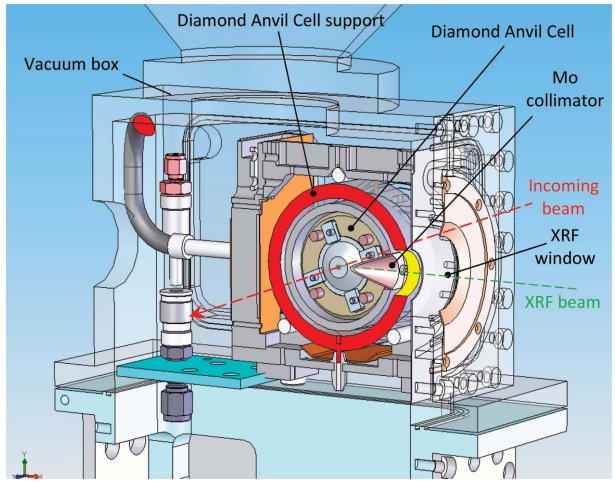

Figure 5
Schematic cross-section view of the HP (10 GPa) and HT (1272 K) diamond anvil cell showing the optimized geometry that allows simultaneous measurements of XRF, XAS and XRD in EH1. The drawing displays the different components: vessel, cooling, feedthroughs, cell holder. The direction of the X-ray beam is also indicated.

geometry that significantly reduces the background radiation (Fig. 5). As a result, for the above-mentioned elements, minimum detection limits of about 0.3 p.p.m. were estimated using such a set-up (Petitgirard *et al.*, 2009). In order to properly handle its 15 kg weight, special translation and rotation stages are incorporated, allowing a precise and robust positioning within the micrometre length scale (MICOS and Huber motors of high repeatability in the micrometre range, with also long travel and submicrometre resolutions). XRD acquisitions in transmission configuration are also suitable over the same high pressure–temperature range.

2.4.2. He mini-cryostat. A compact He mini-cryostat has also been well integrated in EH1. For variable low-temperature investigations (11–300 K) its special technical design provides precise scanning capabilities and allows easy access for multiple detection modes (Martinez-Criado *et al.*, 2007). The chamber is high-purity Al made to avoid background contributions to collected XRF data. To guarantee an extremely short working distance (4.5 mm) and optimized numerical aperture for X-ray excited luminescence studies (Martinez-Criado *et al.*, 2011), the usual thermal shielding used between the sample holder and the window was not included. As a result, the He consumption (13 l d^{-1} at 11 K) is slightly higher than that under standard conditions. The sample change time (60 min), on the other hand, is determined by the long thermal response to warm the system up. Finally, the choice of the window material depends on the wavelength and intensity of radiation, and whether polarization is required. The mini-cryostat not only allows substantial access but also reduces X-ray scattering by eliminating air path (very important for XRF). In addition, electrical contacts are available when transport- and/or electric-field-dependent studies are required.

2.4.3. Linkam stage. Commercially available heating–freezing stages also provide accurate and stable temperatures.

To operate in the 77–873 K range, a HSF91 stage (Linkam Scientific Instruments) compatible with our microprobe set-up is available. The scheme is optimized for vertical mounting and has high temperature stability (<0.1 K). With a compact and versatile design for easy mounting, it is supplied with a thermal jacket for tighter control of the sample environment (kapton or mica windows). The pure silver heating element has even a transverse aperture to accept a quartz capillary loaded with sample. This guarantees the sample is heated from all sides ensuring temperature homogeneity. For operation below room temperature, there is an automated cooling pump with 2 l dewar and 80 cm tube that tolerates a minimum stage temperature of 173 K. The system includes a stand-alone T95-LinkPad system controller with data sampling of 20 times per second. Heating rates can reach up to 150 K min^{-1}. The controller has RS232 connectivity control and programmable outputs for synchronization purposes with our beamline devices.

2.5. Detection schemes

2.5.1. 13-element detector. New requirements in terms of detection limits and acquisition rates fostered the installation and commissioning of a liquid-nitrogen-cooled multi-element Si(Li) detector (Gresham Scientific Instruments, UK) (Letard *et al.*, 2006). Thirteen Si(Li) crystals mounted on a spherical holder form a close-packed array, each element being equidistant from the centre of the sphere. The collimated active area of each crystal is 50 mm^2. It provides a large total active surface (650 mm^2) in optimized compactness (95 mm diameter) without any observable cross-talk effect. The thickness of the crystals is 3.5 mm which preserves the efficiency over the 8–20 keV energy range. The efficiency falls off above 25 keV, with 60% at 30 keV. Each crystal is individually protected by a 12 µm-thick Moxtek DuraBeryllium vacuum window. The digital signal-processing system was manufactured by X-ray Instrumentation Associates (XIA, CA, USA). It is made of four-channel Digital X-ray Processor XMAP modules, designed specifically for quick X-ray mapping (continuous scans). The theoretical maximum throughput is 10^6 counts s^{-1} $channel^{-1}$. However, detection dynamics are significantly reduced by the detector linearity as well as scattering effects. The peaking time can be set between 0.1 and 100 µs. In a high-counting-rate configuration (1 µs peaking time), the linearity measurements showed less than 80 kcounts s^{-1} for a dead-time of about 30% (much lower for a low counting rate, 12 µs peaking time). External triggering can be used for synchronization with other processes such as energy scans or sample motions. The average energy resolution is 150 eV at 5.9 keV (for a peaking time of 12 µs and 1000 counts s^{-1}). The detection limits (for 10 s integration time) are below 0.1 p.p.m. for elements heavier than Mn (Letard *et al.*, 2006).

2.5.2. Silicon drift detectors. Another alternative detection often used in EH1 is the silicon drift detector (SDD) technology. The use of the 13-element detector has been proved to be efficient in many cases (*e.g.* experiments requiring high energy resolution or elemental traces); however, often the relatively low photon count rate of such Si(Li) detectors limits the acquisitions (*e.g.* in XRF tomography). Furthermore, the combination of the high photon flux (>10^{11} photons s^{-1} in the focal spot) and a large variety of sample thicknesses and matrices makes scattering radiation frequently one of the saturation sources. In that context, the complementary SDD technology offers not only lower detection limits and photon count rates at the expense of a slightly decreased energy resolution (150 eV) but also compactness owing to the absence of liquid-nitrogen cooling. In consequence, based on the XIA electronics, two SDDs (Vortex-EX, SII Nano-Technology) are available. The 50 mm^2 single-element SDD produced from high-purity silicon using state-of-the-art CMOS production technology operates with thermoelectric cooling. The drift structure ensures very low capacitance and low noise. In principle, at a peaking time of 0.25 µs, output count rates up to 600 kcounts s^{-1} are achievable. The real count rate measured with 1 µs peaking time is about 175 kcounts s^{-1}.

2.5.3. FReLoN camera for X-ray diffraction. For (powder) diffraction experiments, commonly a large field-of-view camera with low resolution compared with XRF but high quantum efficiency is required. Accordingly, the taper version of the ESRF FReLoN camera (Labiche *et al.*, 2007) is used at the beamline. It consists of a FReLoN F_K4320T (Kodak) equipped with 3.3/1 demagnifying fibre optics taper hardly bonded to the CCD chip (46 µm effective pixel size, 94 mm × 94 mm field of view, sensitivity 1 a.d.u. per incident 20 keV X-ray photon, 0.5 DQE at 20 keV). A 50 µm-thick Gadox powder scintillator screen converts the X-rays into visible-light photons. The use of a Kodak chip offers a high sensitivity of about 3.9 a.d.u. per incident 20 keV X-ray photon and a 0.6 DQE at 20 keV. A microphotodiode is also integrated in the beamstop to record simultaneously the transmitted intensity.

3. Examples of recent scientific applications

The beamline's potential for simultaneous trace-element detection and mapping, quantitative fluorescence analysis, chemical state specificity and structural probe make it ideal for a wide range of disciplines: biology, medicine, environmental and earth sciences, art and archaeology, as well as material sciences. The versatile instrumentation of ID22 offers an excellent scheme to carry out unique projects. The following sections illustrate some of the research activities that have been carried out recently, focused mainly on, but certainly not limited to, the following fields: biomedical, earth and environmental, and materials sciences.

3.1. Biomedical sciences

Various examples of applications include cellular physiology, pharmacology, and toxicology of metal ions involved in biological processes, often called biometals (Bohic *et al.*, 2011; Lewis *et al.*, 2010; Carmona *et al.*, 2010; Bacquart *et al.*, 2010; Ortega *et al.*, 2009; Corezzi *et al.*, 2009). For instance,

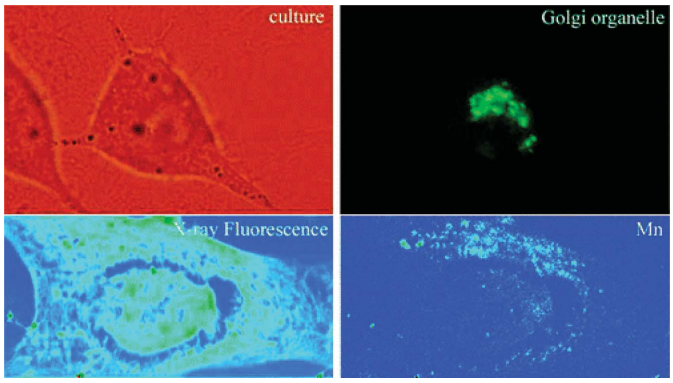

Figure 6
Optical image, visible fluorescence, X-ray fluorescence and Mn elemental distribution in a PC12 cell exposed to 50 μM of $MnCl_2$ for 24 h. The scan size is 5 µm × 5 µm. The colour bar ranges from blue to red (minimum to maximum) and is proportional to the number of X-rays detected. Reproduced with permission from Carmona *et al.* (2010), Copyright 2010 by American Chemical Society.

the biological role of trace elements of Zn and Fe in brain cells has recently been examined by Bohic *et al.* (2011) using nano-XRF on ID22NI. In the report the authors address some of the cellular and molecular processes controlling the entry and distribution of these metals in the brain, as well as their roles in synaptic transmission, in the pathogenesis of some neurologic diseases such as Parkinson's and Alzheimer's diseases, and their impact on cognitive functions.

Another example is the direct speciation analysis of As in sub-cellular compartments by micro-XAS in EH1 with a 10^{-15} g detection limit by Bacquart *et al.* (2010). Their findings show that inorganic arsenite, $As(OH)_3$, is the main form of arsenic in the cytosol, nucleus and mitochondrial network of cultured cancer cells exposed to As_2O_3, whereas As(III) species dominate in HepG2 cells exposed to $As(OH)_3$. On occasion, oxidation to a pentavalent form in nuclear structures of HepG2 cells was observed, suggesting an inter-individual variability in a cell population, that could only be examined by sub-cellular speciation analysis.

In cancer therapy, research has recently been focused on the development of nanocarriers that can aid diagnosis, deliver therapeutic agents and monitor treatment progress. In this context, nano-XRF has been used on ID22NI to investigate intracellular localization of novel lanthanide-coated nanoparticles in human cells and their genotoxicity screening after internalization (Lewis *et al.*, 2010). The results show that, depending on the charge of the coating complex and the presence of the DNA cargo, the internalization of functionalized nanoparticles by human fibroblasts can cause elevated levels of DNA damage. In the same way, applying nano-XRF on ID22NI, Carmona *et al.* (2010) recently found that manganese is located within the Golgi apparatus of PC12 dopaminergic cells at physiologic concentrations (see Fig. 6). Generally, chronic exposure to manganese results in neurological symptoms called manganism, which is identified as a risk factor for Parkinson's disease. Thus, the striking intracellular redistribution of Mn found by Carmona and co-workers indicates that the Golgi apparatus plays an important role in the cellular detoxification of Mn.

3.2. Earth and environmental sciences

The investigations in this area cover exploration from the earth interior up to stellar particles: homogeneity of the deep mantle, fluid–mineral relationships in the upper mantle, tracking elemental speciation in crustal melts and fluid sources in hydrothermal settings, as well as the nature of extra-terrestrial materials (Carbone *et al.*, 2011; Simionovici *et al.*, 2011; Borchert *et al.*, 2010; Petitgirard *et al.*, 2009; Reith *et al.*, 2009). Carbone and co-workers (2011) recently used micro-XRD, micro-XRF and micro-XAS to investigate metal speciation in mine wastes and soils. The authors studied Fe-rich hardpans within waste-rock dump and show that the authigenic iron-rich phases generally contain significant amounts of hazardous elements such as Cu, Zn, Mo, As and Se. Moreover, a significant mineralogical control on the mobility of these elements was observed; in particular, the goethite-rich assemblages show high affinity for Cu and Zn, whereas hematite-rich assemblages selectively concentrate As, Se, Mo, Cu and Zn.

On the other hand, Borchert *et al.* (2010) have examined the partitioning of Ba, La, Yb and Y between haplogranitic melts and aqueous solutions under *in situ* conditions in EH1. Their findings show a strong influence of the composition of the starting fluid and melt with no dependence on temperature and only weak dependence on pressure. For chloridic fluids, there was a sharp increase in the Ba, La, Y and Yb partition coefficients with the alumina saturation index. Their results imply that both melt and fluid compositions have a strong influence on trace-element behaviour, while the complexation of Ba, REEs and Y is not controlled by the presence of Cl in the fluid only, but likely by interaction of these elements with major melt components.

The cycling of rare and precious metals, such as gold, has been also analyzed in ID22NI. In previous studies, researchers reported the presence of bacteria on gold surfaces, but never clearly elucidated their role. Recently, Reith *et al.* (2009) found that the bacterium *Cupriavidus metallodurans* catalyses the biomineralization of gold by transforming toxic gold compounds to their metallic form using an active cellular mechanism. So, there may be a biological reason for the presence of these bacteria on gold grain surfaces. The distribution of gold and other elements was mapped in individual cells (see Fig. 7). After 1 min of exposure to Au(III), cells had taken up 1.82 ng cm^2 of Au, and accumulated Au was distributed throughout the cells. After 72 h, zones containing up to 34.6 ng cm^2 Au were detected. These hot spots were associated with cell envelopes, suggesting that cells actively removed gold from the cytoplasm and precipitated it as nanoparticulate metallic gold in the periplasm. The discovery of an Au-specific means opens the doors to the production of biosensors, which will help mineral explorers to find new gold deposits.

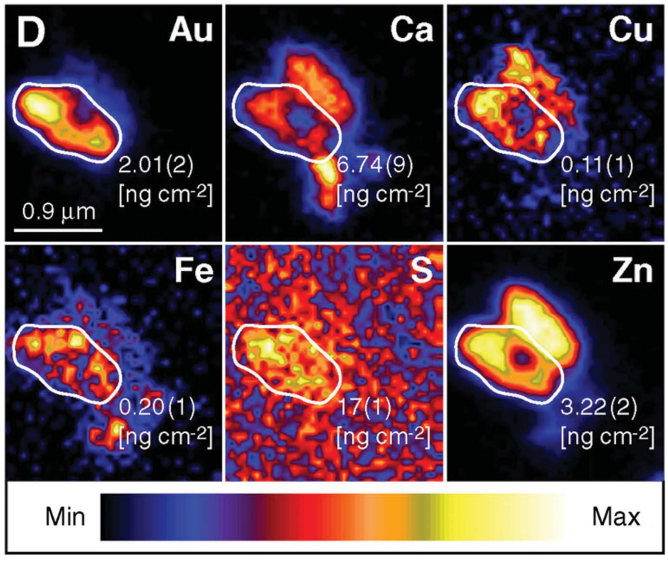

Figure 7
Quantitative micro-XRF maps showing the distribution of Au, Ca, Cu, Fe, S and Zn in an individual cell after 1 min exposure to Au(III) at pH 7.0 [the quantified area is marked in the image, and concentrations and concentration ranges for elements are also given; concentration ranges for elements are: Au, 0–4.16; Ca, 0–18.78; Cu, 0–0.29; Fe, 0–0.44; S, 0–60.52; and Zn, 0–24.57 ng cm^{-2}]. Reproduced with permission from Reith *et al.* (2009), Copyright 2009 by the National Academy of Sciences.

3.3. Materials sciences

In this broad field, several scientific issues have been addressed using the beamline stations. The recent research comprises many materials with potential applications in spintronics, catalysis, optical sources, renewable materials like solid oxide fuel cell and silicon solar cells, *etc* (Sancho-Juan *et al.*, 2011; Basile *et al.*, 2010; Mino *et al.*, 2010; Palancher *et al.*, 2011; Kwapil *et al.*, 2009; Martinez-Criado *et al.*, 2009). For example, the combined use of micro-XRF, micro-XRD and nano-XRF techniques has been applied to the characterization of active-phase-coated metallic supports, structured catalysts, at different scales in both scanning and tomographic modes by Basile *et al.* (2010). In particular, coatings of FeCrAlY foams were examined, which are gaining attention because they improve heat transfer. The results show that the morphology of the coating depends on the synthesis conditions and that the catalyst may be described as Ni metal crystallites dispersed on γ-Al_2O_3, homogeneously coating the FeCrAlY foam.

Another recent experiment applied XRD scanning tomography to an annealed γ-$U_{0.85}Mo_{0.15}$ multiphase particle. UMo/Al dispersion fuel is one of the prospective materials for a high-uranium-density fuel for high-performance research reactors owing to its excellent stability during irradiation. The results published by Palancher *et al.* (2011) revealed a micrometre-scale layered structure morphology, the presence of an embedded 5 µm-thick interdiffusion layer, and an unexpected phase at trace levels which plays a protective role by inhibiting thermally activated Al diffusion into UMo.

The structural characterization of multi-quantum wells in electroabsorption-modulated lasers by Mino *et al.* (2010) is an excellent example of application in the microelectronic industry. The structural gradient (in both strain and barrier/well widths) that allows this system to operate as an integrated device has been determined with a 2 µm × 2 µm beam, scanning both laser and modulator regions. The investigated material is used for 10 Gb s^{-1} telecommunication applications up to 50 km propagation span. In the same way, the application of hard X-ray nanoprobe techniques to the structural analysis of pyramidal defects in Mg-doped GaN, a potential material for optoelectronic devices, has been recently reported (Martinez-Criado *et al.*, 2009). Fig. 8 shows the XRF data collected at ID22NI. The presence of elemental traces of Cr and Fe is revealed. A blue–red plot displays the Cr- and Fe-*K* intensity distributions. While the Ga arrangement presents equally spaced and periodic planes sequentially stacked from the hexagonal base (not shown), Cr and Fe exhibit a close correlation on their spatial locations without the three-dimensional pyramidal shape. The observations emphasize the

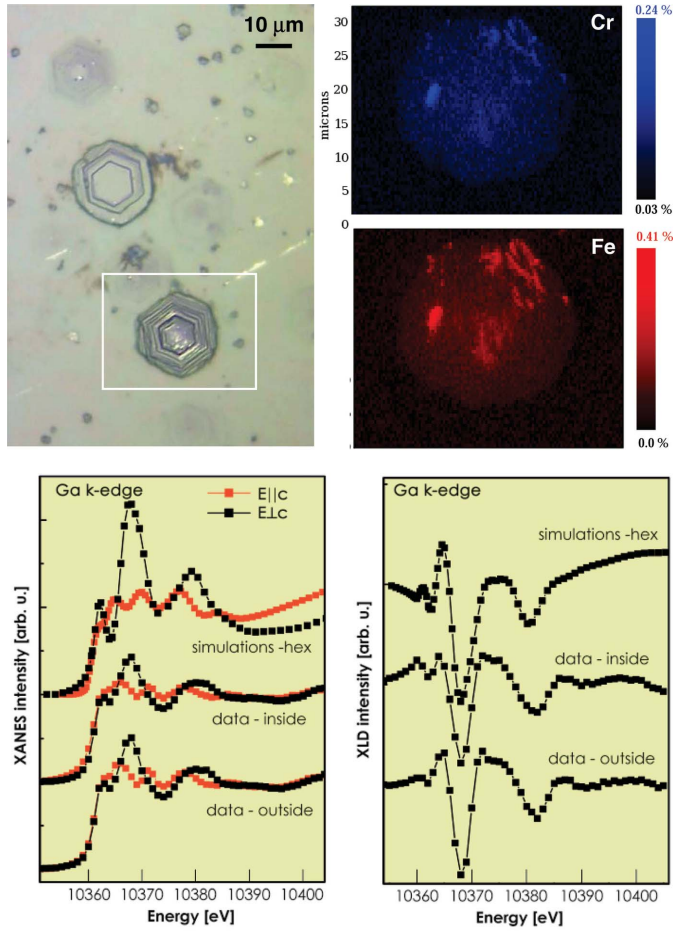

Figure 8
Upper part: optical micrograph of the Mg-rich hexagonal pyramids in GaN and blue–red plot displaying the Cr/Fe *Kα* intensity distributions with their corresponding concentrations in the colour scales. Lower part: calculated and measured XANES data around the Ga *K*-edge for perpendicular/parallel incidence on the pyramid centre and outside it, as well as calculated and measured XLD also recorded at the Ga *K*-edge with the beam focused on the pyramid centre and outside it.

underlying diffusion mechanism, indicating local impurity agglomeration predominantly on the hexagonal base, supporting the occurrence of such pyramids by the kinetics of additional impurities that accompanied Mg incorporation. On the other hand, the strong polarization-dependent XAS features showed the preservation of the hexagonal crystalline structure in both defect-free and hexagonal pyramids. The X-ray linear dichroism (XLD) shows no preferential disorder in the direction parallel or perpendicular to the crystal growth.

4. Long term: upgrade beamline

ID22 will evolve within the frame of the upgrade programme of the ESRF towards the long (185 m) two-branch Nano Imaging and Nano-Analysis (NINA) beamline (http://www.esrf.eu/AboutUs/Upgrade/). The NI end-station will be located at 185 m from the source and will mainly address problems in biology, biomedicine and nanotechnology. It is optimized for high-resolution quantitative 3D imaging techniques with a specific focus on X-ray fluorescence and projection microscopy. This branch will be optimized for ultimate hard X-ray focusing of a beam (10–20 nm) with a large energy bandwidth ($\Delta E/E \simeq 10^{-2}$) at specific energies (11.2, 17 and 33.6 keV). Aiming at life science applications, it will operate in a cryo-environment. The NA end-station, in parallel operation, will be located at approximately 165 m from the source and will be optimized for high-resolution (50 nm to 1 µm) spectroscopic applications ($\Delta E/E \simeq 10^{-4}$), including XRF, XAS and X-ray-excited optical luminescence. It will offer a multi-modal approach (XAS, XRD, XRI) capable of *in situ* experiments. In a complementary way to the NI end-station, NA will provide a monochromatic beam tunable over a large energy range (5–70 keV). The initial development is performed through the station ID22NI under the supervision of P. Cloetens. The NINA beamline will be located on port ID16 and is scheduled to open for users in 2014. In summary, the NINA beamline will provide complementary techniques at the nanoscale for the study of a wide variety of samples, overcoming current ID22 limitations to meet the growing user demands.

5. Conclusions

The ID22 beamline at the ESRF is a state-of-the-art instrument for hard X-ray microanalysis and 2D/3D X-ray imaging at (sub-)micrometre scales. The end-stations suit a large variety of research fields demanding multiple techniques, very tiny spot sizes (from micrometres to 60 nm), high photon flux (up to 5×10^{12} photons s^{-1}) and also high energies (6.5–65 keV). The smooth operation derives from the successful integration of high-quality focusing optics, reliable scanning mechanisms, high-precision mechanical components, efficient detection schemes and stable alignment. Various sample environments allow versatile tailoring of experiments.

Special thanks are due to the machine, instrumentation and technical services of the ESRF for their continuous support. In particular, the authors are very grateful to Joel Chavanne, Yves Dabin, Robert Baker, Eric Gagliardini, Cyril Guilloud, Alejandro Homs, Armando Solé, Jérôme Kieffer and Ricardo Steinmann for their useful and excellent help. GM-C thanks Dr Michael Reynolds for the critical reading of the manuscript.

References

Artioli, G., Cerulli, T., Cruciani, G., Dalconi, M., Ferrari, G., Parisatto, M., Rack, A. & Tucoulou, R. (2010). *Anal. Bioanal. Chem.* **397**, 2131–2136.

Bacquart, T., Deves, G. & Ortega, R. (2010). *Environ. Res.* **110**, 413–416.

Barrett, R., Baker, R., Cloetens, P., Dabin, Y., Morawe, C., Rommeveaux, A., Suhonen, H., Tucoulou, R. & Zhang, L. (2011). *Proc. SPIE*, **8139**, 813904–813912.

Basile, F., Benito, P., Bugani, S., De Nolf, W., Fornasari, G., Janssens, K., Morselli, L., Scavetta, E., Tonelli, D. & Vaccari, A. (2010). *Adv. Funct. Mater.* **20**, 4117–4126.

Bohic, S., Ghersi-Egea, J.-F., Gibon, J., Paolettie, P., Arnaud, J., Hunot, S., Boom, A. & Bouron, A. (2011). *Rev. Neurol.* **167**, 269–279.

Borchert, M., Wilke, M., Schmidt, C., Cauzid, J. & Tucoulou, R. (2010). *Chem. Geol.* **276**, 225–240.

Carbone, C., Marescotti, P., Lucchetti, G., Cauzid, J. & Chalmin, E. (2011). *Neues Jahrb. Mineral. Abh.* **188**, 21–30.

Carmona, A., Deves, G., Roudeau, S., Cloetens, P., Bohic, S. & Ortega, R. (2010). *ACS Chem. Neurosci.* **1**, 194–203.

Cloetens, P. *et al.* (2012). In preparation.

Corezzi, S., Urbanelli, L. & Cloetens, P. (2009). *Anal. Biochem.* **388**, 33–39.

Hignette, O., Cloetens, P., Morawe, C., Borel, C., Ludwig, W., Bernard, P., Rommeveaux, A. & Bohic, S. (2007). *AIP Conf. Proc.* **879**, 792–795.

Kwapil, W., Gundel, P., Schubert, M. C., Heinz, F. D., Warta, W., Weber, E. R., Goetzberger, A. & Martinez-Criado, G. (2009). *Appl. Phys. Lett.* **95**, 232113.

Labiche, J. C., Mathon, O., Pascarelli, S., Newton, M. A., Ferre, G. G., Curfs, C., Vaughan, G., Homs, A. & Carreiras, D. F. (2007). *Rev. Sci. Instrum.* **78**, 091301.

Letard, I., Tucoulou, R., Bleuet, P., Martinez-Criado, G., Somogyi, A., Vincze, L., Morse, J. & Susini, J. (2006). *Rev. Sci. Instrum.* **77**, 063705.

Lewis, D. J., Bruce, C. & Bohic, S. (2010). *Nanomedicine*, **5**, 1547–1557.

Martin, T., Douissard, P.-A., Couchaud, M., Cecilia, A., Baumbach, T., Dupre, K. & Rack, A. (2009). *IEEE Trans. Nucl. Sci.* **56**, 1412–1418.

Martinez-Criado, G., Alen, B., Sans, J. A., Homs, A., Kieffer, I., Tucoulou, R., Cloetens, P., Segura-Ruiz, J., Susini, J., Yoo, J. & Yi, G. (2011). *Nucl. Instrum. Methods Phys. Res. B*, doi:10.1016/j.nimb.2011.08.013.

Martinez-Criado, G., Steinmann, R., Alen, B., Labrador, A., Fuster, D., Ripalda, J. M., Homs, A., Laboure, S. & Susini, J. (2007). *Rev. Sci. Instrum.* **78**, 025106.

Martinez-Criado, G., Tucoulou, R., Cloetens, P., Sans, J. A. & Susini, J. (2009). *Appl. Phys. Lett.* **95**, 151909.

Mino, L., Gianolio, D., Agostini, D., Piovano, A., Truccato, M., Agostino, A., Cagliero, S., Martinez Criado, G., Codato, S. & Lamberti, C. (2010). *Adv. Mater.* **22**, 2050–2054.

Morawe, C., Hignette, O., Cloetens, P., Ludwig, W., Borel, C., Bernard, P. & Rommeveaux, A. (2006). *Proc. SPIE*, **6307**, F3170.

Ortega, R., Bresson, C., Fraysse, A., Sandre, C., Devès, G., Gombert, C., Tabarant, M., Bleuet, P., Seznec, H., Simionovici, A., Moretto, P. & Moulin, C. (2009). *Toxicol. Lett.* **188**, 26–32.
Palancher, H., Tucoulou, R., Bleuet, P., Bonnin, A., Welcomme, E. & Cloetens, P. (2011). *J. Appl. Cryst.* **44**, 1111–1119.
Petitgirard, S., Daniel, I., Dabin, Y., Cardon, H., Tucoulou, R. & Susini, J. (2009). *Rev. Sci. Instrum.* **80**, 033906.
Reith, F., Etschmann, B. & Grosse, C. (2009). *Proc. Natl Acad. Sci. USA*, **106**, 17757–17762.
Sancho-Juan, O., Martinez-Criado, G., Cantarero, A., Garro, N., Salome, M., Susini, J., Olguin, D., Dhar, S. & Ploog, K. (2011). *Phys. Rev. B*, **83**, 172103.
Simionovici, A. *et al.* (2011). *Meteorit. Planet. Sci.* **46**, A213.
Somogyi, A., Tucoulou, R., Martinez-Criado, G., Homs, A., Cauzid, J., Bleuet, P., Bohic, S. & Simionovici, A. (2005). *J. Synchrotron Rad.* **12**, 208–215.
Tucoulou, R., Martinez-Criado, G., Bleuet, P., Kieffer, I., Cloetens, P., Labouré, S., Martin, T., Guilloud, C. & Susini, J. (2008). *J. Synchrotron Rad.* **15**, 392–398.
Vincze, L., Vekemans, B., Brenker, F. E., Falkenberg, G., Rickers, K., Somogyi, A., Kersten, M. & Adams, F. (2004). *Anal. Chem.* **76**, 6786–6791.
Weitkamp, T., Raven, C. & Snigirev, A. (1999). *Proc. SPIE*, **3772**, 311–317.
Zhang, L., Baker, R., Barrett, R., Cloetens, P. & Dabin, Y. (2010). *AIP Conf. Proc.* **1234**, 801–804.